PAPER

Intermittent locomotion of a fish-like swimmer driven by passive elastic mechanism

Bioinspiration & Biomimetics

PAPER

Intermittent locomotion of a fish-like swimmer driven by passive elastic mechanism

RECEIVED
9 May 2018

REVISED
6 July 2018

ACCEPTED FOR PUBLICATION
18 July 2018

PUBLISHED
31 July 2018

Longzhen Dai[1,2], Guowei He[1,2], Xiang Zhang[1,2] and Xing Zhang[1,2]

[1] The State Key Laboratory of Nonlinear Mechanics, Institute of Mechanics, Chinese Academy of Sciences, Beijing 100190, People's Republic of China
[2] School of Engineering Science, University of Chinese Academy of Sciences, Beijing 100049, People's Republic of China

E-mail: zhangx@lnm.imech.ac.cn

Keywords: intermittent swimming, energy efficiency, elastic swimmer, fluid-structure interaction, numerical simulation

Abstract

The intermittent locomotion performance of a fish-like elastic swimmer is studied numerically in this paper. The actuation is imposed only at the head and the locomotion is indirectly driven by passive elastic mechanism. For intermittent swimming, certain time durations of passive coasting are interspersed between two half-periods of active bursting. To facilitate the comparison of energy efficiencies in continuous and intermittent swimming at the same cruising speed, we consider both intermittent swimming at various duty cycles and also continuous swimming at reduced actuation frequencies. The result indicates that the intermittent style is more economical than the continuous style only when the cruising Reynolds number is sufficiently large and the duty cycle is moderate. We also explore the passive tail-beating pattern and wake structure for intermittent swimming. It is found that the kinematics of the tail contains a preparatory burst phase which lies in between the active bursting and the passive coasting phases. Three vortex streets are found in the wake structures behind the intermittent swimmers. The two oblique streets consist of strong vortex dipoles and the horizontal street is made up of weak vortices. The results of this study can provide some insight into the burst-and-coast swimming of fish and also inform the design of efficient bio-mimetic underwater vehicles.

Nomenclature

Dimensional quantities

A^*	amplitude of heaving motion of the head
A^*_{tail}	amplitude of tail flapping motion
B^*	bending rigidity
COT^*	cost of transport per unit mass (energy required for a unit mass to travel a unit distance)
f^*_a	flapping frequency
f^*_0	base flapping frequency for continuous swimming
L^*	body length (reference length for nondimensionlization)
m^*	mass of swimmer
P^*_s	swimming power
t^*	time
T^*	tension coefficient
T^*_a	flapping period ($T^*_a = 1/f^*_a$)
T^*_b	burst time in burst-and-coast swimming (for HT mode, $T^*_b = \frac{1}{2}T^*_a$)
T^*_c	coast time in burst-and-coast swimming
T^*_{cyc}	period of a complete cycle for burst-and-coast swimming (for HT model, $T^*_{cyc} = 2(T^*_b + T^*_c)$)
U^*_c	cruising speed (time-averaged streamwise speed of leading edge)
U^*_{ref}	reference speed for nondimensionlization ($U^*_{ref} = L^* f^*_a$)
Y^*_{head}	lateral position of leading edge
δ^*	thickness of swimmer
λ^*	wave length of body deformation
ν^*	fluid kinematic viscosity
ρ^*_f	fluid density
ρ^*_s	density of swimmer

Dimensionless quantities

$a(t)$	shielding function in time integral for calculating swimming power in burst-and-coast swimming
a_1	mass ratio at leading edge
a_2	dimensionless bending rigidity at leading edge
A	dimensionless amplitude of heaving motion ($A = A^*/L^*$)
A_{tail}	dimensionless amplitude of tail flapping motion ($A_{tail} = A^*_{tail}/L^*$)
b_1	decay factor of mass ratio
b_2	decay factor of dimensionless bending rigidity
$\widehat{COT}$	cost of transport per unit mass normalized by value for continuous swimming driven by base flapping frequency
DC	duty cycle of burst-and-coast swimming ($DC = 1/(1 + T_c/T_b) = 1/T_{cyc}$)
$\boldsymbol{f}$	dimensionless Eulerian forcing vector
$\boldsymbol{F}$	dimensionless Lagrangian forcing vector
m	power index in exponential decay function of mass ratio
n	power index in exponential decay function of dimensionless bending rigidity
p	dimensionless fluid pressure
P_s	dimensionless swimming power
Re_f	flapping Reynolds number ($\mathrm{Re}_f = U^*_{ref}L^*/\nu^* = (L^*)^2 f_0^*/\nu^*$)
Re_c	cruising Reynolds number ($\mathrm{Re}_c = U_c^* L^*/\nu^*$)
s	dimensionless Lagrangian coordinate along arc length
St	Strouhal number
t	dimensionless time
T_a	dimensionless flapping period ($T_a = 1$)
T_b	dimensionless burst time in burst-and-coast swimming (for HT mode, $T_b = \frac{1}{2}$; $T_a = \frac{1}{2}$)
T_c	dimensionless coast time in burst-and-coast swimming
T_{cyc}	dimensionless period of a full cycle in burst-and-coast swimming (for HT mode, $T_{cyc} = 2(T_b + T_c) = 1/DC$)
$\boldsymbol{u}$	dimensionless fluid velocity vector
U	dimensionless swimming speed (instantaneous streamwise speed of leading edge)
U_c	dimensionless cruising speed (time-averaged value of U and $U_c = U_c^*/(L^* f_a^*)$)
$\widehat{U}_c$	cruising speed normalized by value for continuous swimming driven by base flapping frequency
$\boldsymbol{x}$	dimensionless position vector for flow field
$\boldsymbol{X}$	dimensionless position vector for swimmer's body
Y_{tail}	dimensionless lateral position of swimmer's tail
β	mass ratio between swimmer and fluid
γ	dimensionless bending rigidity
θ_{head}	instantaneous pitching angle of leading edge
θ_0	pitching amplitude of leading edge
ξ	dimensionless tension coefficient

1. Introduction

The researches of fish locomotion are largely motivated by (a) the interest in understanding the complex mechanics involved, and (b) using nature for design inspiration for novel underwater vehicles. The experimental studies on live fish have played a vital role in deepening our understanding of the mechanics of fish locomotion. However, some constraints are also encountered in such research works. First, animal locomotion is hard to control and some important physical quantities such as force and torque are hard to measure. Second, it is impossible to isolate the effects of multiple factors on performance by manipulating each control parameter independently. To overcome these difficulties, mechanical devices (or robots) are sometimes used in lieu of live fish in the researches of fish locomotion [1].

Recently, simple mechanical devices which emulate the swimming gaits of fish by utilizing passive elastic mechanisms have received some attention. Unlike the complex robotic fish which provides a close imitation of the biological counterpart [2], this type of device is composed of an elastic panel (or filament) which is actuated at one extremity by heaving or pitching motion (or the combination of the two). The undulatory kinematics which resembles that of a swimming fish is spontaneously produced as a result of fluid-structure interaction (FSI). In an experimental demonstration by Ramananarivo *et al* [3], an elastic swimmer actuated at the head by the magnetic field was shown to locomote on the free surface with an emergent anguilliform kinematics. In a series of studies by Lauder and coauthors, the effects of frequency and amplitude, body length and stiffness, planform and cross-section shape on the propulsive performance were assessed [4–13]. This type of artificial swimmer provides us a useful tool for analyzing flow structure and energy efficiency across a wide range of parameter values.

To date, in all experimental studies which involved such simple fish-like devices, continuous actuation patterns were assumed (imposed driving motions were usually sinusoidal functions of time). It has been well known that besides the continuous (or steady) swimming, intermittent swimming (where the full cycle of actuation consists of both a burst and a coast phase) is another commonly seen locomotion style in many fish species [14], such as northern anchovy [15], golden shiner [16], koi carps [17], cod [18, 19] and zebrafish [20–22]. In fact, the research on intermittent (or burst-and-coast) swimming of fish has a rather long history. The earlier studies on intermittent locomotion of fish

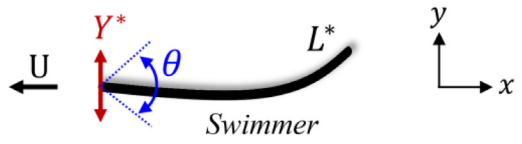

Figure 1. Schematic diagram of the computational model. L^* is the length of the swimmer.

relied on dynamic models with empirical laws for drag. Based on such models, it was unanimously concluded that at the same averaged speed, the intermittent swimming style was superior to the continuous style in terms of energy efficiency [23, 24].

In the recent works on bio-inspired propulsors, however, some disagreements regarding the energy efficiencies of the two different swimming styles have been reported [25–28]. In the experimental study on the pitching-foil systems by Floryan *et al* [25], it was confirmed that the intermittent style enjoyed some advantages in efficiency over the continuous one at the Reynolds number around 10^4. In the inviscid and viscous numerical simulations of pitching-foil systems, it was found that under certain circumstances (such as a sufficiently low Reynolds number or a low duty cycle), continuous swimming can actually be more economical than intermittent swimming [26, 27]. In another viscous simulation of a fish-like swimmer driven by the prescribed undulatory body deformation [28], energy saving in intermittent swimming (in comparison with that in continuous swimming) was confirmed. However, the comparison of energy efficiencies between these two swimming styles at the same averaged speed was not possible since in the problem setting of [28] the continuous swimming style always resulted in a higher speed than the intermittent one.

The wake structure in intermittent swimming was another research focus besides the energy efficiency. In this respect, the placement of vortices behind an intermittent swimmer was found to be very different from that behind a continuous swimmer. Due to the dissimilarities in the swimming gait, the geometric shape and the Reynolds number, the vortex structures in the wakes behind intermittent swimmers were also found to differ from case to case [17, 25–28].

As a natural extension of the studies aforementioned, the intermittent swimming performance of a fish-like swimmer driven by passive elastic mechanism is numerically investigated in this paper. To the best of our knowledge, no such studies have been reported in the literature. We are curious to see if the energy efficiency can be enhanced by switching to an intermittent actuation pattern. Moreover, the wake structure associated with intermittent swimming is also explored.

The rest of the paper is arranged as follows. The computational model and governing equations are presented in section 2. The numerical method, numerical settings and control parameters, together with a mesh-sensitivity test are described in section 3. Some results and discussions regarding the swimming gait, energy efficiency and wake structure are given in section 4. Finally, the conclusions are summarized in section 5.

2. Computational model and governing equations

2.1. Computational model

The fish-like swimmer is modeled as an elastic filament which is actuated at the leading edge by the combination of heaving and pitching motions (see figure 1). In the direction aligned with the x-axis, the swimmer is allowed to move freely without any constraints. With a nonuniform bending rigidity along its body, a carangiform swimming gait (in which substantial undulation only occurs in the posterior part) emerges as the result of FSI.

For continuous swimming, the prescribed heaving and pitching motions at the leading edge are (see figure 2(a)):

$$\begin{cases} Y^*_{head}(t^*) = A^*\cos(2\pi f_a^* t^*) \\ \theta_{head}(t^*) = \theta_0\cos\left(2\pi f_a^* t^* - \frac{\pi}{2}\right) \end{cases}. \tag{1}$$

Here, Y^*_{head} and θ_{head} are the lateral position and pitching angle of the leading edge, respectively. A^* and θ_0 are the amplitudes of the heaving and pitching motions, respectively. Throughout this paper, these two amplitudes are fixed. f_a^* is the flapping frequency (therefore the flapping period is $T_a^* = 1/f_a^*$).

For intermittent swimming, the 'half tail-beating' (HT) mode is assumed here for the actuation (see figure 2(c)). In this mode, certain time durations of passive coasting are interspersed between two half-periods of active bursting. This is in contrast with the 'multiple tail-beating' (MT) mode (see figure 2(b)), where (at least) one period of active bursting is completed before the arrival of passive coasting. Please note that despite of the term '*tail-beating*' used here (such term was conventionally used in some references), the actuation motions in this study are actually only imposed at the *head*.

The kinematics for the burst-and-coast swimming (HT mode) can be written as

$$Y^*_{head}(t^*) = \begin{cases} \frac{1}{4}A^*[\sin(4\pi f_a^* t^*) - 4\pi f_a^* t^*] + \frac{1}{4}A^*\pi, 0 \leqslant t^* < T_b^*; \\ -\frac{1}{4}A^*\pi, \quad T_b^* \leqslant t^* < \frac{1}{2}T_{cyc}^*; \\ -\frac{1}{4}A^*\{\sin[4\pi f_a^*(t^* - T_c^*)] - 4\pi f_a^*(t^* - T_c^*)\} \\ \qquad -\frac{4}{3}A^*\pi, \frac{1}{2}T_{cyc}^* \leqslant t^* < \frac{1}{2}T_{cyc}^* + T_b^*; \\ \frac{1}{4}A^*\pi, \quad \frac{1}{2}T_{cyc}^* + T_b^* \leqslant t^* < T_{cyc}^*; \end{cases}, \tag{2}$$

$$\theta_{head}(t^*) = \begin{cases} \frac{1}{2}\theta_0[1 - \cos(4\pi f_a^* t^*)], \quad 0 \leqslant t^* < T_b^*; \\ 0, \quad T_b^* \leqslant t^* < \frac{1}{2}T_{cyc}^*; \\ -\frac{1}{2}\theta_0\{1 - \cos[4\pi f_a^*(t^* - T_c^*)]\}, \frac{1}{2}T_{cyc}^* \leqslant t^* < \frac{1}{2}T_{cyc}^* + T_b^*; \\ 0, \frac{1}{2}T_{cyc}^* + T_b^* \leqslant t^* < T_{cyc}^*; \end{cases} \tag{3}$$

where T_b^*, T_c^*, T_{cyc}^* are the *burst* time, *coast* time, and the time of a full *burst-coast* cycle respectively. For the

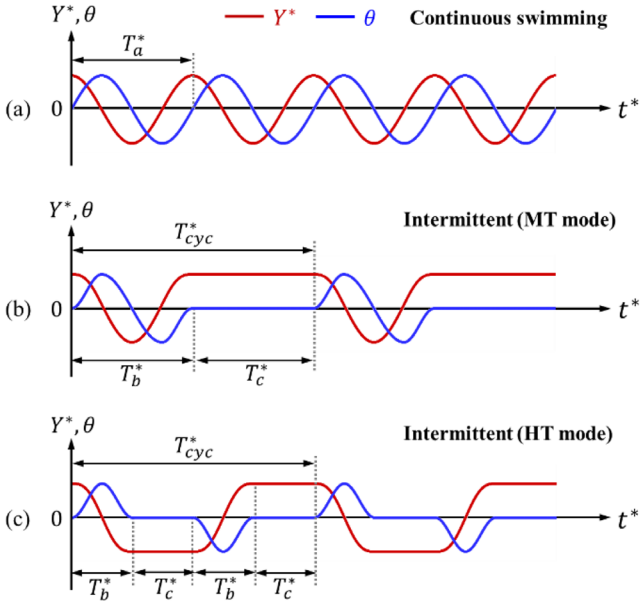

Figure 2. Kinematics of the head for (a) continuous swimming, (b) intermittent swimming (MT mode), and (c) intermittent swimming (HT mode). T_a^* is the flapping period for continuous swimming. T_b^* and T_c^* are the time durations for the active and passive phases of burst-and-coast swimming, respectively. T_{cyc}^* is the time duration of one full cycle in burst-and-coast swimming. In the MT mode of (b), $T_{cyc}^* = T_b^* + T_c^*$ and $T_b^* = T_a^*$. In the HT mode of (c), $T_{cyc}^* = 2\left(T_b^* + T_c^*\right)$ and $T_b^* = 0.5T_a^*$.

HT mode, $T_{cyc}^* = 2\left(T_b^* + T_c^*\right)$ and $T_b^* = 0.5T_a^*$. Please note that smoothed piecewise functions are used here to facilitate a smooth transition between the burst phase and the coast phase (where both the first and second derivatives of Y_{head}^* and θ_{head} exist).

Taking T_a^* as the reference time, the dimensionless counterparts for $T_a^*, T_b^*, T_c^*, T_{cyc}^*$ are denoted by T_a, T_b, T_c, T_{cyc}, respectively. Clearly, $T_a = 1$ and for the HT mode shown in figure 2(c), $T_b = 0.5$. The duty cycle, DC, which represents the degree of intermittency in burst-and-coast swimming, can be defined as:

$$DC = \frac{2T_b}{T_{cyc}} = \frac{1}{1 + \frac{T_c}{T_b}}. \tag{4}$$

As can be seen here, the duty cycle decreases as the intermittency becomes stronger. Since for the HT mode $T_b = 0.5$, the duty cycle can also be expressed as $DC = 1/T_{cyc}$.

Here some additional comments on the computational model adopted in this study are provided. First, the passive elastic mechanism assumed in the model is completely different from the real mechanism at work in fish swimming (where muscles along the body are the primary actuators). However, by tuning the body rigidity in the computational model, the resulted steady swimming gaits can match well with those of fish performing carangiform swimming (to be further addressed in section 3.3). Second, if we compare the body kinematics during the transition from the burst phase to the coast phase in intermittent swimming, subtle difference exists between the present computational model and that of [28]. In [28], the transitional body kinematics was prescribed. In the present computational model, only the transition of the actuation pattern at the head (from 'burst' to 'coast') is prescribed, while the transitional body kinematics is determined by FSI. This subtle difference can lead to a unique preparatory burst gait which is observed in the present study but not reported in [28] (to be further addressed in section 4.2). Since this preparatory burst gait has also been found in the intermittent swimming of real fish, this substantiates the claim that the passive elastic mechanism may play an important role in intermittent swimming. Third, real fish have 3D geometries. However, the study of the 2D model can still provide some useful insight and can also sever as a starting point for further investigation.

2.2. Governing equations

The motions of the fluid and the elastic swimmer are governed by the incompressible Navier–Stokes equations and the nonlinear dynamics equations respectively. The governing equations can be written in a *dimensionless* form as

$$\begin{cases} \frac{\partial \boldsymbol{u}}{\partial t} + \nabla \cdot (\boldsymbol{uu}) = -\nabla p + \frac{1}{\mathrm{Re}_f}\nabla^2 \boldsymbol{u} + \boldsymbol{f}, & (5a) \\ \nabla \cdot \mathbf{u} = 0, & (5b) \end{cases}$$

$$\begin{cases} \beta \frac{\partial^2 \boldsymbol{X}}{\partial t^2} - \frac{\partial}{\partial s}\left(\xi \frac{\partial \boldsymbol{X}}{\partial s}\right) + \frac{\partial^2}{\partial s^2}\left(\gamma \frac{\partial^2 \boldsymbol{X}}{\partial s^2}\right) = -\boldsymbol{F}, & (6a) \\ \frac{\partial \boldsymbol{X}}{\partial s} \cdot \frac{\partial \boldsymbol{X}}{\partial s} = 1. & (6b) \end{cases}$$

Here $\boldsymbol{u}$ is the fluid velocity vector, p is the pressure, and $\boldsymbol{f}$ is the Eulerian forcing term which represents the effect of the immersed body on the flow. The flapping Reynolds number Re_f is defined as $U_{ref}^* L^*/\nu^*$, where L^* is the body length and U_{ref}^* is the reference velocity

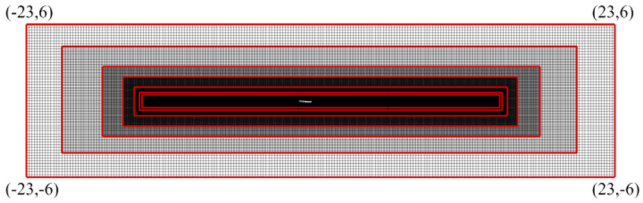

Figure 3. Diagram of the computational domain and the multi-block Cartesian grid used in the simulation.

(which is defined as $L^*f_a^*$), ν^* is the kinematic viscosity of the fluid. $\boldsymbol{X} = (X, Y)$ is the position vector of the swimmer and s is the Lagrangian coordinate along the arc length. $\boldsymbol{F}$ is the Lagrangian force term which presents the interaction between the swimmer and the fluid.

β, ξ, γ are the mass ratio, the dimensionless tension coefficient, and the dimensionless bending rigidity, respectively. The definitions of these dimensionless parameters are:

$$\begin{aligned} \beta &= \frac{\rho_s^* \delta^*}{\rho_f^* L^*}, \\ \xi &= \frac{T^*}{\rho_f^* \left(U_{ref}^*\right)^2 L^*}, \\ \gamma &= \frac{B^*}{\rho_f^* \left(U_{ref}^*\right)^2 L^{*3}}, \end{aligned} \tag{7}$$

where ρ_s^*, ρ_f^* are the densities of the filament and the fluid, respectively. δ^* is the thickness of the filament. T^* and B^* are the (dimensional) tension coefficient and bending rigidity, respectively.

The dimensionless tension coefficient ξ can be determined by solving a Poisson equation to ensure that the inextensible condition (6*b*) is satisfied [29]. Here we assume that the distributions of β and γ along the body can be described by two exponential decay functions:

$$\begin{cases} \beta(s) = a_1 e^{-b_1 s^m}, \\ \gamma(s) = a_2 e^{-b_2 s^n}, \end{cases} \tag{8}$$

where the six coefficients $(a_1, a_2, b_1, b_2, m, n)$ can be adjusted to produce the desirable swimming gaits (to be addressed later in section 3.3).

3. Numerical method and settings

3.1. Numerical method

The direct-forcing immersed boundary method based on the discrete stream function formulation is used to solve the incompressible Navier–Stokes equations (5) [30]. The finite difference method is used to discretize the dynamics equations (6) on a staggered grid [31].

A loosely coupled FSI scheme is used in the simulations of the present study. In this FSI scheme, the fluid equations and dynamics equations are advanced sequentially by one step in time. The procedure of coupling the flow and dynamic solvers within one step (from n to $n+1$) of temporal advancement, including the transfer of data, can be summarized as follows:

(i) The dynamics equations are integrated with the known forcing term of $\boldsymbol{F}$ (at time step n) to obtain the position and velocity of the Lagrangian points (which are used to represent the body of the swimmer). This velocity $\boldsymbol{U}^d$ is treated as the desired velocity of the fluid for imposing the no-slip boundary condition on the swimmer's body.

(ii) The Navier–Stokes equations are integrated without the forcing term $\boldsymbol{f}$ to obtain a tentative solution of fluid velocity $\mathbf{u}^*$. This velocity is then interpolated to the positions of the Lagrangain points to obtain a tentative velocity $\boldsymbol{U}^*$ at the Lagrangian points. A regularized delta function is used as the interpolation kernel function [31].

(iii) The forcing term at the Lagrangian points $\boldsymbol{F}$ (for time step $n+1$) is determined by using $\boldsymbol{U}^*$ and $\boldsymbol{U}^d$. This forcing term is subsequently interpolated to the Eulerian points to obtain the forcing term $\boldsymbol{f}$ for the fluid equations. Again, a regularized delta function is used as the interpolation kernel function [31].

(iv) The Navier–Stokes equations are integrated with the forcing term $\boldsymbol{f}$ to find the fluid velocity at time step $n+1$.

(v) The Lagrangian forcing $\boldsymbol{F}$ for time step $n+1$ is treated as the updated load for the dynamics equations and the integration in step (i) is repeated.

The FSI simulation code used in this work has been extensively validated in [31]. The advantage of the loosely coupled FSI scheme is low computational costs. The limitation of this scheme is that it is only stable when the density ratio β is not to low (i.e. added mass effect is not too strong). Otherwise, instability of this scheme necessitates the use of strongly coupled FSI schemes. In the strongly coupled FSI schemes, the inner iterations between the fluid and dynamics solvers within one step of temporal advancement can result in much higher computational costs.

3.2. Numerical settings

A rectangular computation domain of $[-23, 23] \times [-6, 6]$ is used in the simulation. Here we adopt a multi-block Cartesian mesh with hanging nodes. Comparing with the single-block mesh with stretched elements, this type of mesh can effectively

Table 1. Dimensionless parameters used in simulation of continuous swimming.

Re_f	A	θ_0	a_1	a_2	b_1	b_2	m	n
1000								
2000	0.005	5°	0.1	0.3	3.0	9.0	2.0	2.0
6000								

reduce the total number of grid points while keeping a fair resolution in the vicinity of the swimmer. Seven sub-meshes with different level of refinement are fused into the single mesh used in the simulation (see figure 3). The finest sub-mesh (with the grid spacing of $\frac{L^*}{300}$) is deployed in the sub-domain at the center which occupies the region of $[-14, 14] \times [-0.5, 0.5]$. For all cases studied here, the swimmer never leaves this sub-domain. The grid spacings for other six sub-meshes are $\frac{L^*}{150}$, $\frac{L^*}{75}$, $\frac{2L^*}{75}$, $\frac{4L^*}{75}$, $\frac{8L^*}{75}$, $\frac{16L^*}{75}$ (from the center to the periphery), respectively. The total number of elements in the multi-block Cartesian mesh is about 3 million.

The no-slip boundary condition is imposed on the four outer boundaries of the computational domain. Since the fish-like swimmer is kept at least $5.8L^*$ away from the boundaries during swimming, the blocking effect is negligible. On the surface of the fish-like swimmer, the no-slip boundary condition is enforced by using the direct-forcing immersed boundary technique [31]. The initial fluid velocity is assumed to be zero. Initially, the swimmer's body is kept straight in the direction which aligns to the x-axis and the head is located at its maximum lateral excursion. Time steps for the simulation are chosen such that the *CFL* number based on the maximum fluid velocity and the finest grid spacing never exceeds 0.5.

3.3. Values of control parameters

The dimensionless parameters in the simulation of continuous swimming include: the flapping Reynolds number Re_f, the dimensionless heaving amplitude $A = A^*/L^*$, the pitching amplitude θ_0, and the six coefficients in the exponential decay functions for the bending rigidity γ and the mass ratio β. The values of these parameters are summarized in table 1.

The flapping Reynolds numbers lie in the range of 1000–6000, which is consistent with the values in some studies on fish swimming [17, 21]. Since many burst-and-coast fishes are carangiform swimmers, such as saithe, cod, and zebrafish, here we attempt to emulate the carangiform gaits on the elastic filament. Since noticeable lateral motion is only observed in the posterior part of carangiform swimmers, the values for the kinematic parameters of A and θ_0 are rather small. The coefficients in the exponential decay functions are selected such that the mass ratio and the dimensionless bending rigidity lie in the ranges of $0.1 - 5 \times 10^{-3}$and $0.3 - 3.7 \times 10^{-5}$, respectively. The parameter ranges above are comparable with those of some biological counterparts [6, 18, 32].

The kinematics corresponding to the continuous swimming of the elastic filament at $Re_f = 6000$ is shown in figure 4. The tail-beating amplitude is around $0.12L^*$, which is much larger than the prescribed lateral displacement of the head. This is one typical feature of the carangiform swimming gait [33–35]. From figure 4, it is also seen that roughly 3/4 of a complete wave is displayed on the body length. This indicates that $\lambda^*/L^* \approx 1.33$, where λ^* is the wavelength. This value of the wavelength to body length ratio is consistent with the biological measurements in [36], where the values for carangiform swimmers were found to be larger than unity.

The continuous swimming corresponding to the three flapping Reynolds numbers listed in table 1 are referred to as 'base cases' hereinafter. For each base case, reduced cruising speeds can be achieved by (a) decreasing the driving frequency while keeping the continuous swimming style; or (b) adopting the intermittent swimming style while keeping the driving frequency intact. To facilitate the comparison of performance under the continuous and intermittent swimming conditions at the same cruising speed, two series of simulations are conducted independently for each base case by varying the driving frequency or the duty cycle. The values of the driving frequencies and duty cycles considered in the simulation of this work are listed in table 2. Please note that with the variation of driving frequency under the *continuous* swimming condition, the flapping Reynolds number Re_f and the dimensionless bending rigidity γ should also vary accordingly due to the change of the reference velocity U^*_{ref}.

3.4. Mesh-sensitivity test

To ensure that the results are (approximately) independent of the grid spacing, a mesh-sensitivity test is conducted on the base case of continuous swimming at $Re_f = 6000$. Three meshes of different resolutions are used here (see table 3 for the detailed information).

Figure 5 displays the time histories of the swimming speed obtained by using the three meshes. Here the swimming speed U is defined as the instantaneous streamwise velocity of the leading edge (positive U indicates that the swimmer is moving towards the negative x-direction). From figure 5, it is seen that when reducing the gird spacing from $L^*/200$ to $L^*/300$, significant discrepancy can be found. However, when further reducing the grid spacing from $L^*/300$ to $L^*/400$, the discrepancy is almost negligible (less than 2%). Thus, for all simulation cases in this study, the mesh with the grid spacing of $L^*/300$ is used.

4. Results and discussions

4.1. Metrics of performance

The key parameter to quantify the swimming performance of continuous and intermittent swimming is the cost of transport per unit mass

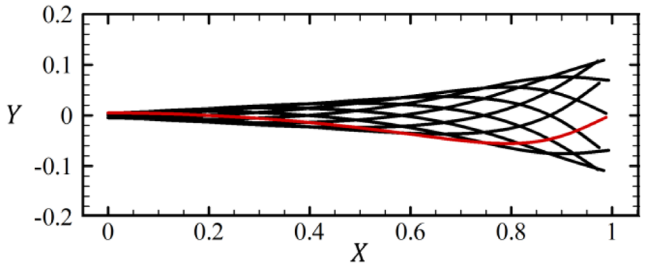

Figure 4. Body kinematics of the fish-like swimmer in continuous swimming at $\mathrm{Re}_f = 6000$ (values of other control parameters are listed in table 1). Ten instantaneous body shapes within one full cycle are superimposed. The body shape marked by red line corresponds to the time when the head is located at its maximum lateral excursion.

Table 2. Values of driving frequencies and duty cycles in simulation.

Base case	Continuous swimming ($DC = 1$)	Intermittent swimming ($f_a^*/f_0^* = 1$)
Re_f	f_a^*/f_0^*	DC
1000	0.2, 0.4, 0.6, 0.8, 1.0	0.2, 0.4, 0.6, 0.8, 0.9, 1.0
2000	0.1, 0.2, 0.4, 0.6, 0.8, 1.0	0.1, 0.2, 0.4, 0.6, 0.8, 0.9, 1.0
6000	0.1, 0.2, 0.4, 0.6, 0.8, 1.0	0.05, 0.1, 0.2, 0.3, 0.4, 0.5, 0.6, 0.7, 0.8, 0.9, 1.0

f_a^*: (dimensional) driving frequencies; f_0^*: (dimensional) base driving frequencies for continuous swimming. The flapping Reynolds numbers Re_f listed in the first column are based on f_0^*.

Table 3. Three meshes used in the mesh-sensitivity test.

Mesh	Minimum grid spacing (L^*)	Total grid cells (million)	Number of sub-meshes
C	1/200	2.2	6
M	1/300	3.0	7
F	1/400	5.6	7

C: coarse mesh; M: medium mesh; F: fine mesh.

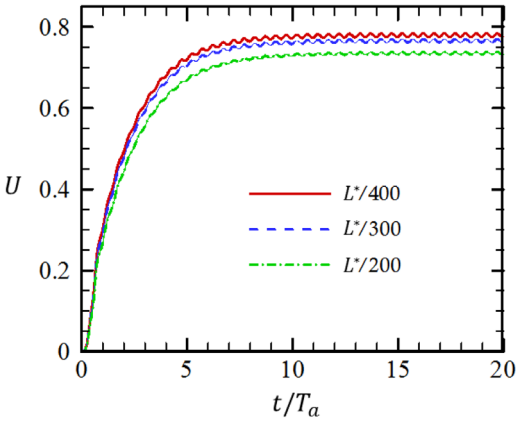

Figure 5. Time histories of the swimming speed obtained by using three meshes with different resolutions.

(energy required for a unit mass to travel a unit distance). This parameter is formally defined as

$$COT^* = \frac{P_s^*}{m^* U_c^*}, \tag{9}$$

where U_c^* is the cruising speed, P_s^* is the swimming power, m^* is the mass of the swimmer. The cruising speed is defined as the time-averaged streamwise velocity of the leading edge. The swimming power is originally defined as the input power needed to maintain the forward swimming and the body undulation. During *active swimming*, the input power can be measured (approximately) by the time-averaged rate at which work is done to the fluid. During the coast phase of intermittent swimming (when the actuation is turned off), the swimming power becomes zero since the input energy ceases to exist. (Although work can still be done to the fluid during coasting, this energy is transformed from the kinetic energy and the elastic potential energy stored in the swimmer's body. Thus, the work done to the fluid can no longer be used to measure the swimming power.)

COT^* is a dimensional quantity with the dimension of acceleration. It is related to the *dimensionless* flow variables by

$$COT^* = L^* (f_a^*)^2 \left[\frac{1}{\int_0^1 \beta(s) ds} \cdot \frac{P_s}{U_c} \right]. \tag{10}$$

Here P_s and U_c are the dimensionless swimming power and cruising speed, respectively. The definitions of these two quantities are:

$$P_s = \frac{1}{T} \int_0^T a(t) \left[\int_0^1 \left(\boldsymbol{F} \cdot \frac{\partial \boldsymbol{X}}{\partial t} \right) ds \right] dt, \tag{11}$$

$$U_c = -\frac{1}{T} \int_0^T \left(\frac{\partial X}{\partial t}\bigg|_{s=0} \right) dt. \tag{12}$$

For continuous swimming, the averaging is performed over one flapping period (i.e. $T = T_a = 1$). For intermittent swimming, the averaging is performed

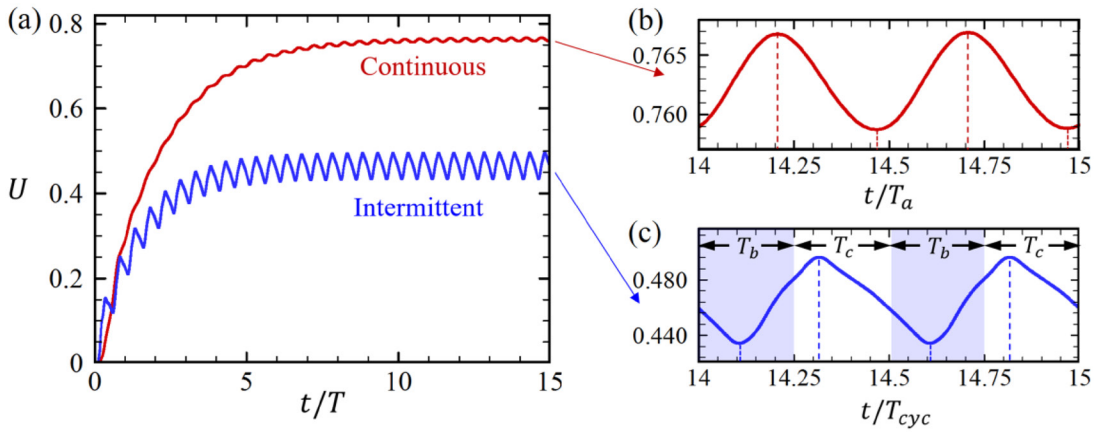

Figure 6. (a) Time histories of the swimming speeds of the leading edge for the two types of swimming (positive value corresponds to motion along the negative x-direction). Red line: basic case of continuous swimming at $\mathrm{Re}_f = 6000$ ($T = T_a$); blue line: burst-and-coast swimming of $DC = 0.5$ at $\mathrm{Re}_f = 6000$ ($T = T_{cyc}$). (b) Enlarged view of the swimming speed within one period of time for continuous swimming. (c) Enlarged view of the swimming speed within one full cycle for burst-and-coast swimming. The vertical dashed lines in (b) and (c) correspond to the time when the maximum or minimum velocities are reached. The shaded regions with light blue color in (c) correspond to the time durations of the burst phase in the actuation.

over the entire cycle (i.e. $T = T_{cyc} = 1/DC$). In addition, for intermittent swimming only the work done to the fluid during the *burst phase* is reckoned in. Thus, the shielding function $a(t)$ in (11) is defined as

$$a(t) = \begin{cases} 0, & \text{if} \quad DC \neq 1.0 \ \ \& \ \ t \in \text{coast interval}, \\ 1, & \text{otherwise}. \end{cases} \tag{13}$$

In this study, we are interested in accessing the performances of the swimmer when performing continuous and intermittent swimming at the same cruising speed. To this end, we define the *normalized COT* and the *normalized* cruising speed by normalizing COT^* and U_c^* using the corresponding reference quantities of the base cases (i.e. continuous swimming driven by frequency f_0^*):

$$\widehat{COT} = \frac{COT^*}{COT^*|_{DC=1}^{f_0^*}} = \frac{\frac{1}{\int_0^1 \beta(s)ds} \cdot \frac{P_s}{U_c}}{\left[\frac{1}{\int_0^1 \beta(s)ds} \cdot \frac{P_s}{U_c}\right]\Big|_{DC=1}^{f_0^*}} \cdot \left(\frac{f_a^*}{f_0^*}\right)^2, \tag{14}$$

$$\hat{U}_c = \frac{U_c^*}{U_c^*|_{DC=1}^{f_0^*}} = \frac{U_c}{U_c|_{DC=1}^{f_0^*}} \cdot \left(\frac{f_a^*}{f_0^*}\right). \tag{15}$$

The Strouhal number, which relates the tail flapping amplitude, the flapping frequency and the cruising speed, is an important dimensionless number used to describe the kinematics of animal locomotion (including swimming and flying). This dimensionless number can also be linked with the energy efficiency in animal swimming and flying. The Strouhal number is defined as

$$\mathrm{St} = \frac{2A_{tail}^* f_a^*}{U_c^*} = \frac{2A_{tail}^* f_a^*}{f_a^* L^* U_c} = \frac{2\bar{A}_{tail}}{U_c}, \tag{16}$$

and

$$\begin{aligned} \mathrm{St} &= \frac{2A_{tail}^*(1/T_{cyc}^*)}{U_c^*} = \frac{2A_{tail}^*(1/T_{cyc}^*)}{L^* f_a^* U_c^*} \\ &= \frac{2\bar{A}_{tail}}{U_c} \cdot \frac{T_a^*}{T_{cyc}^*} = \frac{2\bar{A}_{tail}}{U_c} \cdot DC \end{aligned}, \tag{17}$$

for continuous swimming and intermittent swimming, respectively. Here A_{tail}^* and $\bar{A}_{tail}$ are the dimensional and dimensionless tail flapping amplitudes, respectively.

4.2. Swimming speed and gait

In this section, we compare the speed and gait in continuous and intermittent swimming.

Figure 6 shows the time histories of instantaneous speeds for continuous and intermittent swimming at $\mathrm{Re}_f = 6000$. The DC value for intermittent swimming is 0.5. It can be seen that the averaged swimming speed decreases roughly by 40% at $DC = 0.5$, when comparing with that of continuous swimming. For continuous swimming, the time history of velocity is a sinusoidal function as expected. For intermittent swimming, it is seen that the velocity time history possesses the sawtooth-shaped waveform. This is the typical velocity pattern which manifests itself in the intermittent swimming of fish [23]. From the velocity history shown in figure 6(c), a phase shift between the periodic variation of velocity and that of the imposed actuating motion at the head is clearly seen. After the flapping motion of the head is initiated, there is a delay of $0.4T_b$ before the swimmer starts to accelerate. The acceleration lasts about $0.8T_b$ and is followed by a time duration of deceleration which lasts about $1.2T_b$. It is interesting to note that asymmetry in the velocity history exists in terms of the time durations for acceleration and deceleration (although the time durations for the active and the passive phases in the actuation are equivalent).

The kinematics of the body for intermittent swimming at $DC = 0.5$ is shown in figure 7. If compared with the kinematics of the body for continuous swimming shown in figure 4, it is seen that envelopes of the body shapes in these two cases are almost the same. However, how the 'net' is woven by the instantaneous body shapes is very different. The difference in

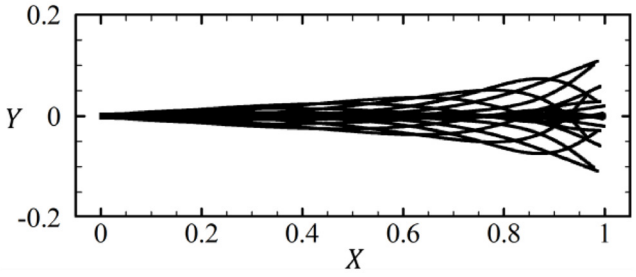

Figure 7. The swimming gait of the fish-like swimmer operating at $DC = 0.5$ and $\mathrm{Re}_f = 6000$. Twenty instantaneous body shapes within one full cycle are superimposed.

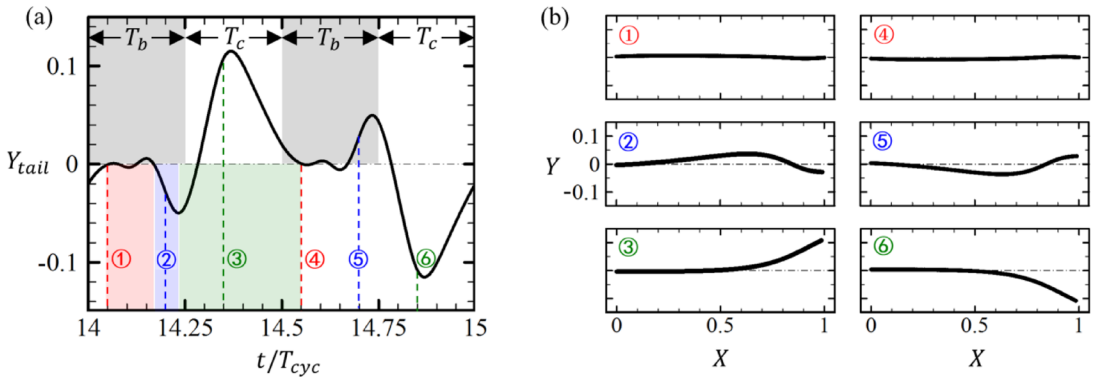

Figure 8. (a) Lateral position of the tail as a function of time within one full cycle of burst-and-coast swimming at $DC = 0.5$. (b) Six snapshots of instantaneous body shapes corresponding to the three distinct phases within one cycle. The six dashed lines and numbers in (a) denote the time instants of the six snapshots shown in (b). The shaded regions with grey color in (a) correspond to the time durations of the burst phases in the actuation. The pink, blue and green colors in (a) represent the time durations of the coast, the preparatory burst and the burst phases in the kinematics of the tail.

the kinematics can be further revealed by examining the time history of the lateral position of the tail (see figure 8). For continuous swimming, the tail oscillates in a sinusoidal fashion (same as the prescribed motion of the head in waveform but with a larger amplitude and a phase shift). For intermittent swimming, the tail's motion becomes more complicated (in comparison with the prescribed head motion shown in figure 2(c)). From figure 8(a), we can see that the tail's kinematics within half full cycle can be broken down into three distinct phases: (a) coast with an approximate straight posture, (b) preparatory burst with one tail flick and (c) burst with two tail flicks. Please note that the unique preparatory burst gait is an emergent feature of the system due to the combined effect of elasticity and FSI. Six snapshots of the instantaneous body shapes corresponding to the three distinct phases within one full cycle are illustrated in figure 8(b).

From figures 6(c) and 8(a), it can be seen that the swimming speed reaches its maximum value at roughly the same time as the tail reaches its maximum lateral excursion. This is consistent with the findings in [17], where experiments were conducted to investigate the burst-and-coast swimming of koi carps. In the experiments by Videler and Weihs [24] on the burst-and-coast swimming of cod and saithe, a three-phase swimming gait similar to that shown in figure 8(b) was also found. Interestingly, this swimming gait shares some similarities with the rapid starting gaits of slender fish [37].

4.3. Energy efficiency

In this section, we assess performances of continuous and burst-and-coast swimming by comparing the energy efficiencies at the same cruising speed.

In figure 9, the normalized *COT* is plotted as a function of the normalized cruising speed, for the three flapping Reynolds numbers listed in table 2. At $\mathrm{Re}_f = 1000$ (where the cruising Reynolds number $\mathrm{Re}_c = (U_c^* L^*)/\nu^*$ ranges from 110 to 400), the continuous style outperforms the intermittent style in general. The efficiency gap between the two swimming styles is very narrow at high *DC* values. This gap almost shrinks to zero around $DC = 0.7$ and becomes slightly wider at very low *DC* values. At $\mathrm{Re}_f = 2000$ (where Re_c ranges from 80 to 1100), the efficiency gap between the two swimming styles is rather narrow for the entire range of *DC*. The intermittent style marginally outperforms the continuous style for $0.4 < DC < 0.8$. At $\mathrm{Re}_f = 6000$ (where Re_c ranges from 400 to 4600), the intermittent style markedly outperforms the continuous style for $0.3 < DC < 0.85$. The widest gap between the two is found at $DC = 0.6$, where the normalized COT of the intermittent style is 25% less than that of the continuous style.

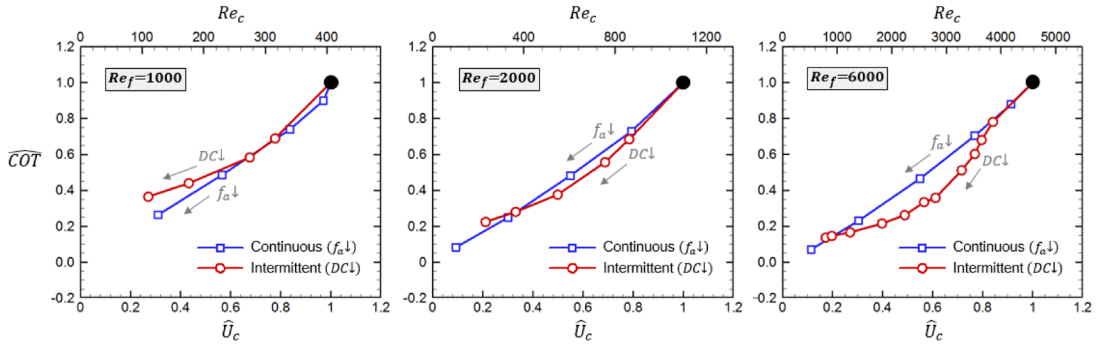

Figure 9. Normalized cost of transport as a function of normalized cruising speed in burst-and-coast swimming and continuous swimming. The three plots are for the three cases with flapping Reynolds number of 1000, 2000 and 6000, respectively. The blue lines with hollow blue squares denote a series of continuous swimming cases with reduced driving frequencies. The red lines with hollow red circles denote a series of burst-and-coast swimming cases with reduced duty cycles. The filled black circles in these plots denote the three base cases of continuous swimming (where the cruising velocity and *COT* are used as reference quantities for normalization). The cruising Reynolds number shown in the plots is defined as $\mathrm{Re}_c = (U_c^* L^*)/\nu^*$.

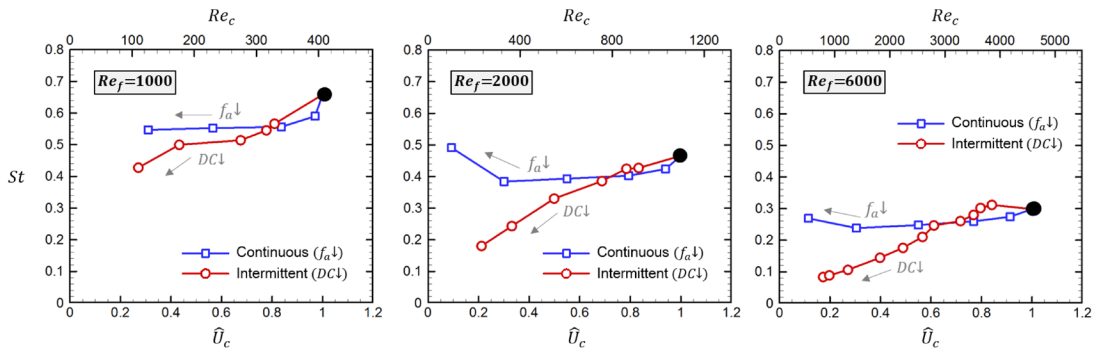

Figure 10. Strouhal number as a function of normalized cruising speed in burst-and-coast swimming and continuous swimming. The three plots are for the three cases with flapping Reynolds number of 1000, 2000 and 6000, respectively. The blue lines with hollow blue squares denote a series of continuous swimming cases with reduced driving frequencies. The red lines with hollow red circles denote a series of burst-and-coast swimming cases with reduced duty cycles. The filled black circles in these plots denote the three base cases of continuous swimming. The cruising Reynolds number shown in the plots is defined as $\mathrm{Re}_c = (U_c^* L^*)/\nu^*$.

The results shown in figure 9 indicate that the intermittent style becomes more economical than the continuous style only when the cruising Reynolds number is relatively high and the *DC* value is moderate. This finding can be used to rationalize the observations that the intermittent style is seldom adopted by larva fish [15, 21, 38–41] or fish cruising at low speeds [18]. In the study of intermittent swimming of koi carps [17], significant efficiency enhancement was achieved for $2500 < \mathrm{Re}_c < 3000$. This range of cruising Reynolds number is consistent with the finding of this work.

Here we would also like to compare the result of the present study with some recent numerical studies on the intermittent swimming of *rigid* pitching foils. In an inviscid simulation, it was demonstrated that the intermittent style can be less economical than the continuous style at sufficiently low *DC* values [26]. In a viscous simulation [27], similar trend as that shown in figure 9 was found in the *COT*-*U* plots for the Re_c range of 3000–7000. The maximal *COT* reduction by switching from continuous to intermittent gait was found to be around 20% [27].

In figure 10, the Strouhal number (St) is plotted as a function of the normalized cruising speed, for the three flapping Reynolds numbers listed in table 2. It is seen that at $\mathrm{Re}_f = 1000$, the St numbers lie in the range of $0.43 < \mathrm{St} < 0.66$. Clearly, the St numbers are out of the narrow range of $0.2 < \mathrm{St} < 0.4$, in which many swimming and flying animals cruise [42, 43]. However, there are also evidences which support that the Strouhal number can vary over a relatively larger range of $0.6 < \mathrm{St} < 2.2$, for anguilliform and low Reynolds number undulatory swimmers [44, 45]. At $\mathrm{Re}_f = 2000$, the St numbers lie in the range of 0.18–0.49. The St numbers for most data points are within or close to the narrow range for animal locomotion. At $\mathrm{Re}_f = 6000$, the range of St numbers becomes $0.08 < \mathrm{St} < 0.3$. The data points for continuous swimming and also intermittent swimming at intermediate and high DC values lie within the narrow range for animal locomotion.

4.4. Wake structure

The wake structures behind the swimmer at various *DC* values are compared in figure 11. Since the wake structures are not very sensitive to the Reynolds number (at least for the parameter range considered in this work), only the results for $\mathrm{Re}_f = 6000$ are

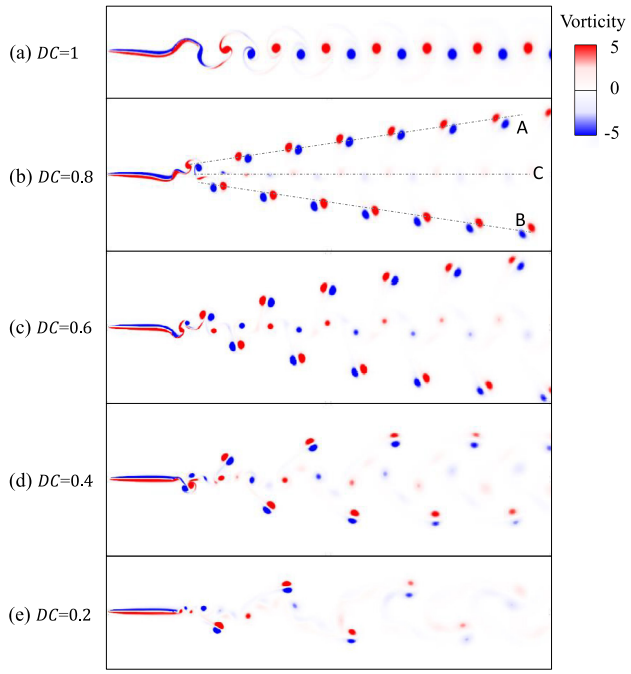

Figure 11. Instantaneous vorticity contours of the fluid field for continuous swimming (a) and burst-and-coast swimming (b)–(e) at $\mathrm{Re}_f = 6000$. Red and blue indicate the positive (anti-clockwise oriented) and negative (clockwise oriented) vorticities.

presented. For the continuous style ($DC = 1.0$), one pair of vortices are shed from the tail within one flapping period and a reverse Karman vortex street is formed in the wake. For the intermittent style ($DC < 1.0$), *six* vortices are shed within one complete cycle. These vortices are positioned along three straight lines (vortex streets) in the wake, and are denoted as 'A', 'B' and 'C' in figure 10(b), respectively. The two oblique vortex streets (A) and (B) are composed of a series of strong vortex dipoles. The horizontal vortex street (C) is composed of a series of vortices which are significantly weaker in strength. This type of wake structure leads to a symmetry velocity profile with respect to the centerline and a zero averaged lateral force. By comparing the wake structures for intermittent swimming at different *DC* values, it appears that the duty cycle has no effect on the overall pattern of the wake (such as the number of vortices formed within one complete cycle). The duty cycle does have some influences on the spatial arrangement of the vortices (such as the inclination angles of the oblique vortex streets and the spatial distance between two successive dipoles). For sufficiently low *DC* values, vortex streets A and B tend to orient themselves horizontally in the far wake. The interspacing between two successive dipoles is found to increase with decreasing *DC* values. In addition, the duty cycle also has a noticeable impact on the strength of the vortices in vortex street C. The vortex strength in C reaches the maximum at a moderate *DC* value around 0.6.

To clearly visualize the evolution of vortex structure during intermittent swimming at $DC = 0.5$ and $\mathrm{Re}_f = 6000$, twelve snapshots of the instantaneous vorticity field within one complete cycle are presented in figure 12. The four stronger (primary) vortices which are organized into two dipoles (2–3 and 5–6) are formed during the burst phase. The increase of interspacing between the two successive dipoles in vortex streets A and B with decreasing *DC* can thus be explained by the increase of time interval between two successive active burst motions. During the coast phase, two thin shear layers with concentrated vorticity are attached to the body. The two weaker (secondary) vortices (1 and 4) in vortex street C are then produced during the preparatory burst phase due to vorticity pinch-off. The reasons why a moderate *DC* value results in the maximum vortex strength in vortex street C are as follows. First, very small *DC* leads to a low cruising speed, which attenuates the vorticity strength in the shear layers. Second, very large *DC* leads to a short gliding (coasting) distance, which prevents the vorticity from accumulating in the shear layers.

The emergence of two vortex dipoles within one complete cycle is largely consistent with the experimental observation on the HT-mode intermittent swimming of koi carps [17]. However, vortex street C was not found in the experiment of [17]. The lack of the weaker vortices in the experiment can be attributed to the lack of preparatory burst phase or the insufficient resolution for capturing such structures. The wake structure observed here differs markedly from those produced by swimmers performing MT-mode intermittent swimming [17, 25–28]. In the experiments on the MT-mode intermittent swimming of koi carps and rigid pitching foils [17, 25], *two* primary vortices were generated per cycle (just like the wake structures for continuous swimming). In the experiments on pitching foils, *two* secondary vortices were also observed [25]. In the computational studies on the MT-mode intermittent swimming of rigid

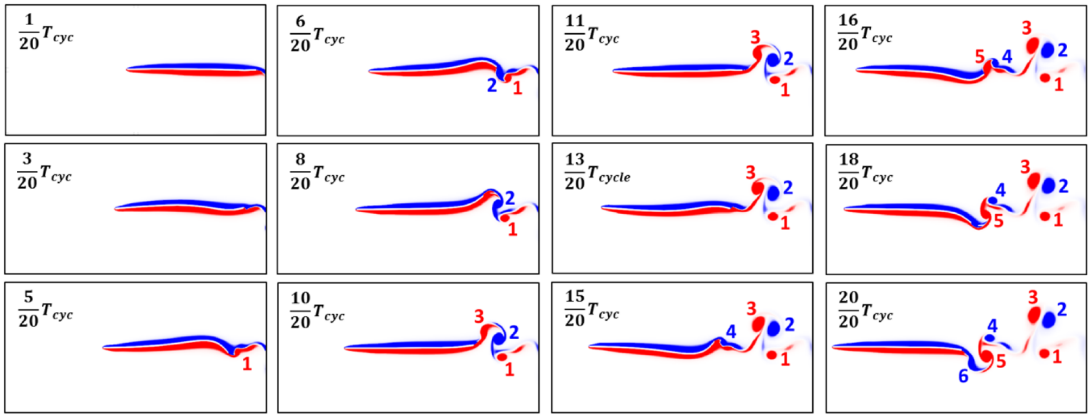

Figure 12. Successive snapshots of the instantaneous vorticity contours within one flapping cycle T_{cyc} for burst-and-coast swimming of $DC = 0.5$ and $\mathrm{Re}_f = 6000$. Color bar is the same as figure 11.

pitching foils and fish-like swimmers [26–28], it was found that *three* primary vortices were shed per cycle. Beside the primary vortices aforementioned, *one* secondary (weak) vortex was also found in the studies of [26, 27]. The wake structures found in [26–28] can lead to asymmetric time-averaged velocity profiles (with respect to the centerline). This implies that the swimmers may experience non-zero averaged lateral forces. Thus, from the perspective of bio-mimetic design, the HT mode is preferable to the MT mode in the sense that counteracting lateral forces are not needed during intermittent swimming.

5. Conclusions

Numerical simulations are conducted in this work to assess the intermittent locomotion performance of a fish-like swimmer driven by passive elastic mechanism. The continuous locomotion at three different flapping Reynolds numbers are selected as the base cases. For each base case, two series of simulations are conducted by (a) maintaining the duty cycle of unity while reducing the flapping frequency, and (b) maintaining the flapping frequency while reducing the duty cycle (increasing intermittency of the actuation). This facilitates the comparison between energy efficiencies for the continuous and the intermittent swimming styles at the same cruising speed.

The results on efficiency indicate that the intermittent style is more economical than the continuous style only when the cruising Reynolds number is sufficiently large and the duty cycle value is moderate. This finding is consistent with the observations that larval fish or fish in low-speed cruising seldom adopt the intermittent swimming style. The trends of efficiency variation with the changes of Reynolds number and duty cycle observed here also agree well with those obtained in the studies of bio-inspired propulsors.

A preparatory burst phase of the tail is discovered in the intermittent locomotion of the fish-like swimmer. This unique swimming gait is an emergent feature of the system due to the combined effect of elasticity and FSI. Similar tail motions have also been found in live fish when performing intermittent swimming or rapid starting maneuvers. The emergence of the preparatory burst gait in this study also suggests that the passive elastic mechanism may play an important role in the intermittent swimming of fish.

The wake structure for the HT-mode intermittent swimming consists of three vortex streets. The two oblique vortex streets are composed of strong vortex dipoles which are formed during the active burst phase of the tail motion. The horizontal vortex street is composed of weak vortices which are formed during the preparatory burst phase. This vortex structure is in general consistent with the observations on live fish when performing HT-mode intermittent swimming.

The results of this study can provide some insight into the burst-and-coast swimming of fish and also inform the design of efficient bio-mimetic underwater vehicles.

Acknowledgments

We thank D Weihs for the helpful discussion during his visit to IMECH (CAS). This work was supported by Chinese Academy of Sciences under Projects No. KJCX-SW-L08, KJCX3-SYW-S01 and XDB22040104, National Natural Science Foundation of China under Projects No. 11772338, No. 10732090, No. 11023001, No. 11232011, No. 11372331.We would like to thank the National Supercomputing Center in Tianjin (NSCC-TJ) for the allocation of computing time.

ORCID iDs

Xing Zhang https://orcid.org/0000-0002-4960-0221

References

[1] Lauder G V 2015 Fish locomotion: recent advances and new directions *Annu. Rev. Mar. Sci.* 7 521–45

[2] Flammang B E, Tangorra J L, Mignano A P and Lauder G V 2017 Building a fish: the biology and engineering behind a bioinspired autonomous underwater vehicle *Mar. Technol. Soc. J.* **51** 15–22
[3] Ramananarivo S, Godoy-Diana R and Thiria B 2013 Passive elastic mechanism to mimic fish-muscle action anguilliform swimming *J. R. Soc. Interface* **10** 20130667
[4] Lauder G V, Anderson E J, Tangorra J and Madden P G A 2007 Fish biorobotics: kinematics and hydrodynamics of self-propulsion *J. Exp. Biol.* **210** 2767
[5] Lauder G V, Madden P G A, Tangorra J L, Anderson E and Baker T V 2011 Bioinspiration from fish for smart material design and function *Smart Mater. Struct.* **20** 094014
[6] Lauder G V, Lim J, Shelton R, Witt C, Anderson E and Tangorra J L 2011 Robotic models for studying undulatory locomotion in fishes *Mar. Technol. Soc. J.* **45** 41–55
[7] Lauder G V, Flammang B and Alben S 2012 Passive robotic models of propulsion by the bodies and caudal fins of fish *Integr. Comp. Biol.* **52** 576
[8] Shelton R M, Thornycroft P J M and Lauder G V 2014 Undulatory locomotion of flexible foils as biomimetic models for understanding fish propulsion *J. Exp. Biol.* **217** 2110
[9] Feilich K L and Lauder G V 2015 Passive mechanical models of fish caudal fins: effects of shape and stiffness on self-propulsion *Bioinspir. Biomim.* **10** 036002
[10] Lucas K N, Thornycroft P J M, Gemmell B J, Colin S P, Costello J H and Lauder G V 2015 Effects of non-uniform stiffness on the swimming performance of a passively-flexing, fish-like foil model *Bioinspir. Biomim.* **10** 056019
[11] Lim J L and Lauder G V 2016 Mechanisms of anguilliform locomotion in fishes studied using simple three-dimensional physical models *Bioinspir. Biomim.* **11** 046006
[12] Saadat M, Fish F E, Domel A G, Santo V D, Lauder G V and Haj-Hariri H 2017 On the rules for aquatic locomotion *Phys. Rev. Fluids* **2** 083102
[13] Zhu R *et al* 2017 Propulsive performance of pitching panels with bio-inspired passive directional flexibility *AIAA Paper 2017-3980 (47th AIAA Fluid Dynamics Conf.)* (https://doi.org/10.2514/6.2017-3980)
[14] Kramer D L and McLaughlin R L 2001 The behavioral ecology of intermittent locomotion *Amer. Zool.* **42** 137–15
[15] Weihs D 1980 Energetic significance of changes in swimming modes during growth of larval anchovy, Engraulis mordax *Fish. Bull.* **77** 597–604
[16] Fish F E, Fegely J F and Xanthopoulos C J 1991 Burst-and-coast swimming in schooling fish (Notemigonus Crysoleucas) with implications for energy economy *Comp. Biochem. Physiol.* **100A** 633–7
[17] Wu G H, Yang Y and Zeng L J 2007 Kinematics, hydrodynamics and energetic advantages of burst-and-coast swimming of koi carps (Cyprinus carpio koi) *J. Exp. Biol.* **210** 2181–91
[18] Videler J J 1981 Swimming movements, body structure and propulsion in cod Gadus morhua *Symp. Zool. Soc. Lond.* **48** 1–27
[19] Blake R W 1983 Functional design and burst-and-coast swimming in fishes *Can. J. Zool.* **61** 2491–4
[20] Fuiman L A and Webb P W 1988 Ontogeny of routine swimming activity and performance in zebra danios (Teleostei: Cyprinidae) *Anim. Behav.* **36** 250–61
[21] Muller U K, Stamhuis E J and Videler J 2000 Hydrodynamics of unsteady fish swimming and the effect of body size: comparing the flow fields of fish larvae and adults *J. Exp. Biol.* **203** 193–206
[22] McHenry M J and Lauder G V 2005 The mechanical scaling of coasting in zebrafish (Danio rerio) *J. Exp. Biol.* **208** 2289–301
[23] Weihs D 1974 Energetic advantages of burst swimming of fish *J. Theor. Biol.* **48** 215–29
[24] Videler J and Weihs D 1982 Energetic advantages of burst-and-coast swimming of fish at high speeds *J. Exp. Biol.* **97** 169–78
[25] Floryan D, Buren T V and Smits A J 2017 Forces and energetics of intermittent swimming *Acta Mech. Sin.* **33** 725–32
[26] Akoz E and Moored K W 2018 Unsteady propulsion by an intermittent swimming gait *J. Fluid Mech.* **834** 149–72
[27] Moored K, Akoz E, Liu G, Han P and Dong H 2017 Disentangling the inviscid and viscous energy saving mechanisms of intermittent swimming *AIAA Paper 2017-3981 (47th AIAA Fluid Dynamics Conf.)* (https://doi.org/10.2514/6.2017-3981)
[28] Chung M H 2009 On burst-and-coast swimming performance in fish-like locomotion *Bioinspir. Biomim.* **4** 1–12
[29] Huang W X, Shin S J and Sung H J 2007 Simulation of flexible filaments in a uniform flow by the immersed boundary method *J Comput. Phys.* **226** 2206–28
[30] Wang S Z and Zhang X 2011 An immersed boundary method based on discrete stream function formulation for two- and three-dimensional incompressible flows *J. Comput. Phys.* **230** 3479–99
[31] Zhu X J, He G W and Zhang X 2014 Numerical study on hydrodynamic effect of flexibility in a self-propelled plunging foil *Comput. Fluids* **97** 1–20
[32] McHenry M J, Pell C A and Long J H 1995 Mechanical control of swimming speed: stiffness and axial wave form in undulating fish models *J. Exp. Biol.* **198** 2293–305
[33] Ashraf I, Godoy-Diana R, Halloy J, Collignon B and Thiria B 2016 Synchronization and collective swimming patterns in fish (Hemigrammus bleheri) *J. R. Soc. Interface* **13** 1–9
[34] Videler J J and Hess F 1984 Fast continuous swimming of two pelagic predators, saithe (Pollachius virens) and mackerel (Scomber scombrus): a kinematic analysis *J. Exp. Biol.* **109** 209–28
[35] Videler J J 1993 *Fish Swimming* (Berlin: Springer)
[36] Lindsey C C 1978 *Form, Function and Locomotory Habits in Fish Fish Physiology Vol. VII Locomotion* ed W S Hoar and D J Randall (New York: Academic) pp 8–26
[37] Weihs D 1973 The mechanism of rapid starting of slender fish *Biorheology* **10** 343–50
[38] Hunter J R 1972 Swimming and feeding behaviour of larval anchovy Engraulis mordax *Fish. Bull.* **70** 821–38
[39] Vlymen W J 1974 Swimming energetics of the larval anchovy, Engraulis mordax *Fish. Bull.* **72** 885–99
[40] Batty R S 1984 Development of swimming movements and musculature of larval herring (Clupea harengus) *J. Exp. Biol.* **110** 217–29
[41] Osse J W M and Drost M R 1989 Hydrodynamics and mechanics of fish larvae *Pol. Arch. Hydrobiol.* **36** 455–65
[42] Triantafyllou M S, Triantafyllou G S and Gopalkrishnan R 1991 Wake mechanics for thrust generation in oscillating foils *Phys. Fluids* **3** 2835–7
[43] Taylor G K, Nudds R L and Thomas A L R 2003 Flying and swimming animals cruise at a Strouhal number tuned for high power efficiency *Nature* **425** 707–11
[44] Muller U K, van den Boogaart J G M and van Leeuwen J L 2008 Flow patterns of larval fish: undulatory swimming in the intermediate flow regime *J. Exp. Biol.* **211** 196–205
[45] van Weerden J F, Reid D A P and Hemelrijk C K 2014 A meta-analysis of steady undulatory swimming *Fish Fish.* **15** 397–409